Fundamental limit of phonon Tesla valve for heat rectification from first principles

Huan Wu and Yongjie Hu*
School of Engineering and Applied Science, University of California, Los Angeles, Los Angeles, California, 90095, USA

(Received 8 September 2025; accepted 20 March 2026; published 18 May 2026)

Directional control of heat remains a central challenge for energy conversion, waste-heat utilization, and thermal management, as existing thermal rectifiers exhibit low efficiency or operate only at cryogenic temperatures. Here we demonstrate giant phonon rectification in solid-state "phonon Tesla valves", inspired by Nikola Tesla's fluidic one-way valve but governed by fundamentally different transport physics. Using *ab initio* Boltzmann transport simulations with full scattering matrices, we show that hydrodynamic phonon transport in graphite coupled with asymmetric valve geometry produces strong forward-backward contrast in phonon relaxation. Single-stage devices achieve rectification ratios of up to approximately 8, while multistage configurations reach ratios of approximately 16, far exceeding those of prior thermal diodes. The rectification mechanism originates from asymmetric relaxation of nonequilibrium phonons at diffusive boundaries, in contrast to inertia-driven fluid Tesla valves. These results examine the performance limits of phonon Tesla valves and establish a platform for directional heat control and highlight the unique potential of hydrodynamic phonons for thermal information processing and energy technologies.

DOI: 10.1103/bgr6-wryy

I. INTRODUCTION

The manipulation of matter and energy has defined each technological revolution. While fluids and electrons are routinely controlled, the directional control of heat remains a central challenge with transformative potential in energy conversion, waste-heat recovery, and thermal management [1–8]. Most existing thermal rectifiers either exhibit low rectification ratios (less than 2) or operate only under cryogenic conditions [9–11], leaving solid-state thermal diodes far from practical relevance.

Here we introduce and quantitatively analyze a solid-state "phonon Tesla valve," inspired by Nikola Tesla's fluidic one-way valve that was invented in 1920 [12]. Unlike its fluid counterpart, where rectification is limited by particle number conservation, phonon rectification leverages the unique relaxation dynamics of collective, driftlike phonon transport. Recent experimental advances have achieved rectification ratios of approximately 15% [13]. Here, using *ab initio* simulations that capture mode-resolved scattering beyond the relaxation-time approximation (RTA), we demonstrate that geometric optimization enables rectification ratios approaching approximately 16 in multistage designs, representing a nearly 2 orders of magnitude improvement beyond prior thermal diodes.

II. HYDRODYNAMIC PHONON TRANSPORT

In fluids, mass transport occurs via bulk drift motion characterized by a velocity field. By contrast, in solids heat usually transport diffusively, governed by Fourier's law [14]. Hydrodynamic phonon transport represents an intermediate regime in which phonons move collectively in a driftlike manner, analogous to fluid flow [15–21]. Unlike classical diffusion driven solely by phonon density gradients [22], the hydrodynamic regime sustains bulk drift, producing a parabolic heat flux profile reminiscent of Poiseuille flow [Fig. 1(a)], in contrast to the uniform profile of diffusion [Fig. 1(b)].

The hydrodynamic regime arises when momentum-conserving normal processes dominate over momentum-destroying Umklapp scattering [23]. In a three-phonon process, if $\mathbf{q}+\mathbf{q}'$ remains inside the Brillouin zone [Fig. 1(c)], momentum is conserved (normal process); if it is outside, folding back destroys momentum [Fig. 1(d)], causing a Umklapp process. Most materials, such as silicon, are Umklapp process dominated and therefore diffusive, whereas graphite exhibits strong normal processes that drive hydrodynamic transport [20,24–26].

A key manifestation is the scattering angle dependence of scattering rates $\gamma(\theta)$,

$$\gamma(\theta) = \frac{\sum_\lambda C_\lambda \gamma_\lambda(\theta)}{\sum_\lambda C_\lambda}, \tag{1}$$

*Contact author: yhu@seas.ucla.edu

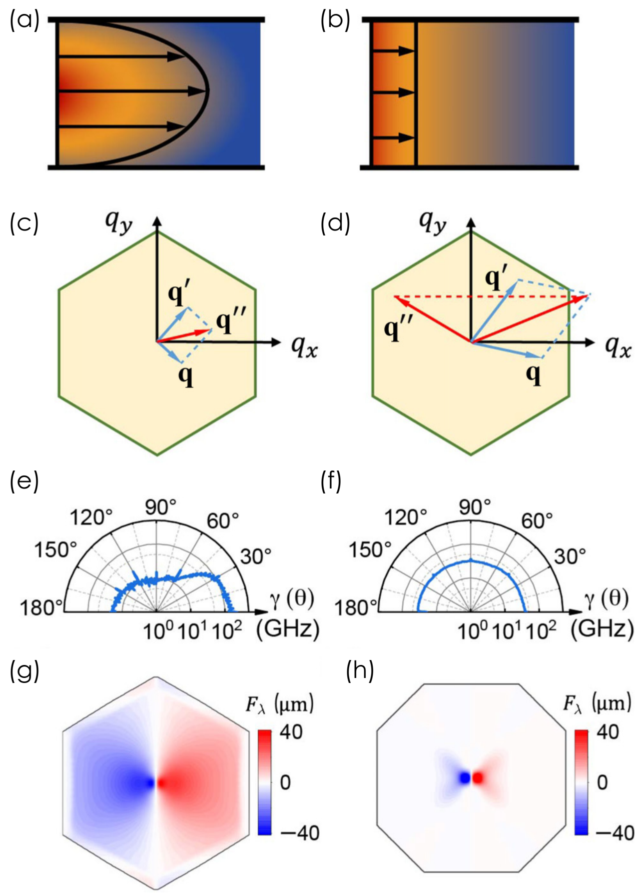

FIG. 1. Hydrodynamic phonon transport in graphite due to strong normal scattering. (a) Hydrodynamic transport and (b) diffusive transport. (c) Normal process and (d) Umklapp process. (e),(f) Scattering angle–dependent scattering rates of (e) graphite and (f) silicon at 100 K. (g),(h) Deviation from equilibrium Bose-Einstein distribution $F_{x,\lambda}$ driven by ∇T for (g) graphite out-of-plane acoustic branch and (h) silicon transverse acoustic branch at 100 K, cutoff at the $q_z = 0$ plane.

$$\gamma_\lambda(\theta) = 2\pi \left| \sum_{\lambda' \neq \lambda} \Omega_{\lambda',\lambda} \frac{\omega_{\lambda'}}{\omega_\lambda} \delta(\theta - \theta_{\lambda',\lambda}) \right|, \tag{2}$$

where $\lambda \equiv (\mathbf{q}, s)$ labels a phonon mode of wave vector $\mathbf{q}$ and polarization s, and C_λ and ω_λ denote its volumetric specific heat and frequency, respectively. $\theta_{\lambda',\lambda}$ is the angle between the group velocities of λ and λ', and $\Omega_{\lambda',\lambda}$ is the scattering matrix [27]. The factor $\omega_{\lambda'}/\omega_\lambda$ balances the energy during the mode transition. *Ab initio* calculations of $\gamma(\theta)$ reveal that in graphite at 100 K scattering is strongly biased forward [Fig. 1(e)], preserving the propagation direction and enabling sustained drift. By contrast, Si exhibits nearly isotropic $\gamma(\theta)$ due to dominant Umklapp processes [Fig. 1(f)], which rapidly restore equilibrium.

To quantify the nonequilibrium nature of hydrodynamic transport, we calculate the deviation coefficient $\mathbf{F}_\lambda$ by solving the Boltzmann transport equation beyond the relaxation-time approximation [28]. $\mathbf{F}_\lambda$ measures the deviation of the phonon distribution n_λ from equilibrium (n_λ^0) driven by the temperature gradient ∇T, defined by $n_\lambda = n_\lambda^0 + (-\partial n_\lambda^0/\partial T)\mathbf{F}_\lambda \cdot \nabla T$. In graphite, $|F_{\lambda,x}|$ for the flexural acoustic branch exceeds 10 μm across much of the Brillouin zone [Fig. 1(g)], indicating large deviation from the Bose-Einstein distribution. In contrast, in silicon, $|F_{\lambda,x}|$ is below 0.1 μm for most of the area [Fig. 1(h)], reflecting rapid equilibration. These results establish that strong normal scattering in graphite sustain great deviation from an equilibrium distribution, enabling advectionlike drift behavior central to phonon Tesla valves.

III. PHONON TESLA VALVE DESIGN

By using the advection nature of the driftlike phonon transport in graphite and combining it with the design of the Tesla valve, we propose a phonon Tesla valve as a thermal rectifier to manipulate heat flow. The design of the phonon Tesla valve is shown in Fig. 2(a). We take the flow direction from the top-left corner to the bottom-right corner as forward, and the reverse direction as backward. When a heat source is placed at the top-left corner, the heat flow is driven in the forward direction, splitting into two channels and undergoing complex processes before reaching the outlet. Conversely, when the heat source is placed at the bottom-right corner, the heat flow in the backward direction proceeds more straightforwardly. According to our calculations, the forward direction has larger thermal resistance than the backward direction, leading to thermal rectification.

IV. METHOD

To quantify the rectification effect, we rigorously compute the phonon transport by accurately capturing collective driftlike motions through a comprehensive treatment of phonon scattering, extending beyond the conventionally adopted RTA. In most common materials such as silicon, the RTA is typically applied to describe the phonon scattering, where relaxation times are assigned to phonon modes to represent the time interval between consecutive scatterings, disregarding the angular dependence of scattering. However, in graphite, the phonon scattering exhibits significant angular dependence due to strong normal scattering, resulting in failure of the RTA. To address this, the linearized three-dimensional Boltzmann transport equation (BTE) is solved with full consideration of the scattering matrix $\Omega_{\lambda,\lambda'}$ that quantifies the phonon transition rates from λ' to λ:

$$\frac{\partial \delta n_\lambda}{\partial t} + \mathbf{v}_\lambda \cdot \nabla \delta n_\lambda = \sum_{\lambda'} \Omega_{\lambda,\lambda'} \delta n_{\lambda'}, \tag{3}$$

where $\delta n_\lambda = n_\lambda - n_\lambda^0$ is the deviation of the nonequilibrium phonon distribution n_λ from the equilibrium

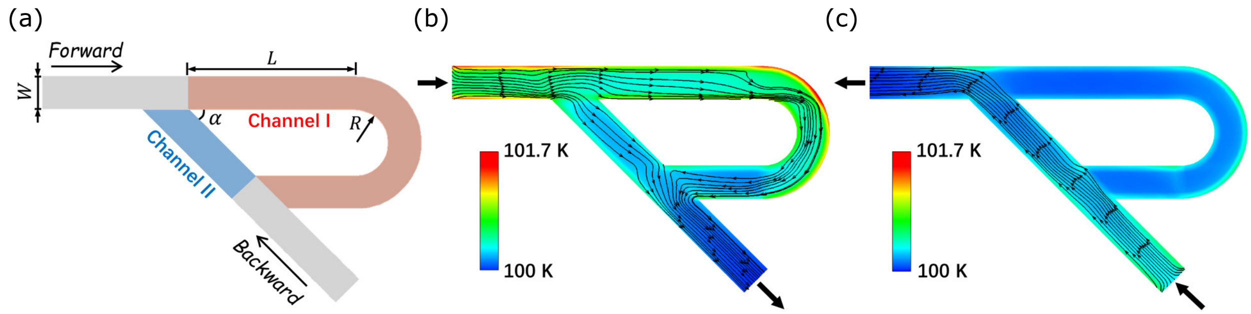

FIG. 2. Phonon Tesla valve design and transport dynamics. (a) Design of phonon Tesla valve. (b),(c) Temperature distribution and heat flux streamlines under a heating power of 1 mW at the inlet boundary for (b) forward flow and (c) backward flow. The color map shows the temperature, the curves represent the streamlines, and the arrows indicate the flow directions. The streamlines for channel I are not shown in (c) due to negligible heat flux density. The channel width is 100 nm.

Bose–Einstein distribution n_λ^0, and $\mathbf{v}_\lambda$ is the group velocity of mode λ. If we retain only the diagonal elements of $\Omega_{\lambda,\lambda'}$ and set the off-diagonal elements to zero, the scattering term on the right-hand-side of Eq. (3) reduces to the RTA. In this work, we retain the off-diagonal elements of $\Omega_{\lambda,\lambda'}$, which is beyond the RTA. The scattering matrix of isotopically pure graphite is determined by an *ab initio* approach [27,28]. The only inputs of the *ab initio* approach are the interatomic force constants (IFCs), which are extracted by fitting of the irreducible displacement-force set with the use of ALAMODE [29], with interatomic forces determined by density functional theory [30,31] with the use of Quantum ESPRESSO [32,33]. The scattering matrix is derived from the IFCs on the basis of quantum perturbation theory [27]. The numerical settings for obtaining the scattering matrix for isotopically pure graphite are the same as in our previous work [20]. Projector-augmented-wave pseudopotentials were used in the density functional theory calculations [34]. The nonlocal exchange-correlation functional vdW-DF-ob8 was used to accurately account for the long-range van der Waals interatomic interactions in graphite [35]. The kinetic energy cutoff for electronic wave functions was 120 Ry. The structure was relaxed with the use of the primitive cell with Monkhorst-Pack grids of $14 \times 14 \times 6$. The IFCs were derived from a 588-atom supercell with Monkhorst-Pack grids of $2 \times 2 \times 2$. The cutoff radius for the third-order IFCs was 9 bohr. The mesh of the $\mathbf{q}$ points for phonon transport was $50 \times 50 \times 8$.

The three-dimensional mode-dependent BTE is difficult to solve in a Tesla valve due to the intricate mode dependencies and transitions, as well as the complex structure of the valve. To efficiently solve Eq. (3), we use a variance-reduced Monte Carlo algorithm [20,36] that solves the BTE in the form of deviational energy:

$$\frac{\partial \delta f_\lambda}{\partial t} + \mathbf{v}_\lambda \cdot \nabla \delta f_\lambda = \sum_{\lambda'} A_{\lambda,\lambda'} \delta f_{\lambda'}, \tag{4}$$

where $\delta f_\lambda = \hbar\omega_\lambda \delta n_\lambda$ is the deviational energy and $A_{\lambda,\lambda'} = \Omega_{\lambda,\lambda'}\omega_\lambda/\omega_{\lambda'}$ is the matrix that describes the energy exchange between phonon modes through phonon scattering. The motion and scattering of each sample particle, which carries unit energy contributing to the deviation from equilibrium, are simulated on the basis of the BTE. The energy carried by sample particles is sampled to derive the temperature deviation from the background temperature. Within this deviational energy–based framework, computational efficiency is increased and stochastic uncertainty is reduced, as the scattering inherently conserves energy and the sampling focuses on the small deviations from the equilibrium background [6,20,36,37].

All boundaries are diffusive, where the sample particle randomly changes its mode according to the equilibrium distribution, and the velocity is updated according to the new mode. Within the deviational energy–based framework, the mode is updated at diffusive boundaries according to the distribution of the mode-dependent specific heat C_λ, since the deviational energy contained by phonon mode λ under an equilibrium temperature rise ΔT is $C_\lambda \Delta T$. The heat flux is driven by a temperature gradient ∇T applied at the inlet boundary, where sample particles are initialized following the distribution $|C_\lambda \mathbf{v}_\lambda \cdot \nabla T|$. The outlet boundary is fixed at the background temperature, where the sample particles are removed upon arrival, as δf_λ vanishes there. The numerical implementations for all types of boundary conditions are designed to be compatible with the deviational energy–based formalism, with details provided in Ref. [20].

The thermal resistance is derived as the temperature difference between the inlet area and the outlet area (see Fig. 7 in Appendix A for locations) divided by the heating power. Since the BTE is linearized, the model provides the temperature rise relative to the equilibrium background, which is proportional to the heating power. This linearization assumption provides results in the limit of small temperature differences.

To validate our model, we compare it with recent experimental measurements conducted at 45 K on devices with a channel width of 4.5 μm, thickness of 90 nm, and angle of 35°, where a rectification ratio γ of 1.152 was reported. For better alignment with experimental conditions, we account for the mix of specular and diffusive reflection by applying Ziman's model [27,38] to estimate the probability of specular reflection at the side boundaries. Although Ziman's model simplifies the complex boundary reflection process, it captures the qualitative trend of a monotonically varying γ with surface roughness, and we choose surface roughness of 2.48 Å to achieve quantitative agreement with experiment. Under the same geometry and temperature as in experiment, our calculation gives γ of 1.154, showing good agreement with the experimental observation.

V. RESULT AND DISCUSSION

A. Single-stage valve

Figures 2(b) and 2(c) show the calculated temperature distributions and heat flux streamlines for a single-stage valve. In the forward direction, a large portion of the heat flux passes through channel I, undergoes a U-turn, and merges with the flow in channel II. The phonon flow from channel I attempts to go back through channel II, but is overwhelmed by the upstream flow in channel II. In the backward direction, the flow passes directly through channel II without experiencing much tortuosity. Therefore, the thermal resistance is different between the forward and backward directions, resulting in thermal rectification. The performance of thermal rectification is quantified by the rectification ratio defined as $\gamma = R_f/R_b$, where R_f and R_b are the thermal resistances of the forward and backward directions, respectively. The calculated γ is 2.66 for the design in Fig. 2 with a channel width W of 100 nm.

The rectification effect requires sufficient thickness, as the diffusive scattering at the top and bottom boundaries can impede the driftlike phonon flow. In Fig. 3(a), we examine γ under various thicknesses for the valve structure in Fig. 2, showing that γ decreases from 2.66 to 2 as the thickness is reduced from 100 μm to 10 nm. In general, the phonon transport shows distinct behavior at a reduced characteristic length scale. When the length scale becomes comparable to or smaller than the intrinsic phonon mean free path, which is the average distance a phonon travels between successive internal scatterings, such as anharmonic and isotope scatterings, the phonon propagates ballistically between the channel walls with minimal scattering. This ballistic transport is analogous to radiation and is fundamentally different from diffusive and hydrodynamic transport. To analyze the thickness effect, we calculate the cumulative in-plane thermal conductivity $\kappa_{x,\mathrm{cum}}$ as a function of cross-plane mean free path Λ_z, where $\Lambda_{\lambda,z} = |v_{\lambda,z}|\tau_\lambda$, where $v_{\lambda,z}$ and τ_λ are the cross-plane

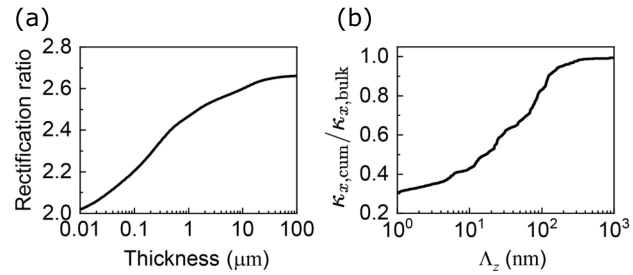

FIG. 3. Thickness dependence. (a) Rectification ratio as a function of thickness. (b) Normalized cumulative bulk in-plane thermal conductivity $\kappa_{x,\mathrm{cum}}$ as a function of cross-plane phonon mean free path Λ_z.

group velocity and the relaxation time of mode λ, respectively. As shown in Fig. 3(b), phonons with $\Lambda_{\lambda,z}$ greater than 10 nm contribute 70% of the in-plane thermal conductivity. When the thickness becomes smaller than $\Lambda_{\lambda,z}$, phonons undergo ballistic transport between the top and bottom surfaces. In this regime, diffusive boundary scattering at the surfaces restores the phonons toward the equilibrium distribution, impeding the phonon flow and weakening the rectification effect. For thickness greater than 50 μm, reduction of the thickness does not significantly increase the number of phonons with $\Lambda_{\lambda,z}$ exceeding the thickness, leading to only a mild decrease in γ. However, once the thickness drops below 1 μm, the fraction of ballistic phonons rises sharply, resulting in a pronounced reduction in γ. Nevertheless, the rectification effect persists even at an extremely small thickness of 10 nm, with γ remaining as high as 2. This is because phonons with $\Lambda_{\lambda,z}$ less than 10 nm still contribute around 30% of the in-plane thermal conductivity, as modes with very small cross-plane velocities (e.g., $|v_{\lambda,z}| < 0.01$ m/s) can also have relatively large in-plane group velocities and thus contribute significantly to in-plane thermal transport. To create a clean condition for studying other effects besides thickness in the follow-up investigations, we eliminate its influence by setting the thickness to 100 μm, which is far greater than the cross-plane mean free paths.

To systematically investigate the rectification effect, we adjust the geometric parameters of the phonon Tesla valve, including the angle α between the two channels, the channel width W, and the channel I length L, as illustrated in Fig. 2(a). We examine γ for various α values, with W, R, and L fixed at 100 nm, 100 nm, and 1.5 μm, respectively. Figure 4(a) shows a maximum γ value of approximately 3 occurring at $\alpha = 45°$. For the forward direction, as α increases, fewer phonons leak through channel II, which tends to increase R_f. But a large α value also makes the phonons in channel I less likely to flow back through channel II due to the increased deflection angle, which tends to reduce R_f. In addition, the increasing α value increases the length ratio between channels I and II, tending to increase

R_f/R_b. These competing effects result in a maximum γ value at $\alpha = 45°$.

To investigate the size effect, we uniformly scale down the Tesla valve structure, with the degree of scaling represented by the overall length of the valve L_{overall}, as shown in Fig. 4(b). When L_{overall} exceeds 100 μm, γ drops below 1.05, and is expected to approach 1 with further increases in size, as phonon transport becomes increasingly diffusive at larger scales. As the dimensions scale down, γ keeps increasing, and reaches approximately 6 when L_{overall} is reduced to 0.4 μm. This trend may appear counterintuitive, as the hydrodynamic effect is typically suppressed at the ballistic limit, where the phonon mean free path exceeds the channel width. To understand this behavior, we separately examine the influence of channel width W and channel I length L on γ.

To isolate the effect of channel width on rectification, we vary W while fixing all other geometric parameters, including $R = 20$ nm, $\alpha = 45°$, and $L = 0.3$ μm. As shown in Fig. 4(c), γ increases as W decreases, which seems to be counterintuitive, particularly at narrow widths such as 20 nm. One might expect the rectification effect to weaken, as the phonon mean free paths greatly exceed the channel width. In this regime, ballistic transport between diffusive boundaries is intuitively expected to suppress the directional phonon flow, and diminish the rectification effect.

To understand why γ keeps increasing with decreasing W, we begin by examining the distribution of the phonon mean free path component perpendicular to the channel walls (Λ_y) relative to the channel width. This distribution is characterized by the cumulative bulk thermal conductivity along the channel length direction $\kappa_{x,\text{cum}}$ as a function of Λ_y. Here $\Lambda_{\lambda,y} = |v_{\lambda,y}|\tau_\lambda$, where $v_{\lambda,y}$ and τ_λ are the group velocity component perpendicular to the channel wall and the relaxation time of phonon mode λ, respectively. The channel length direction is chosen to align with the armchair orientation of graphite. As shown in Fig. 4(d), phonons with $\Lambda_{\lambda,y} < 20$ nm still contribute 18% of the total thermal conductivity, as some phonon modes have group velocities nearly parallel to the channel wall and with a very small $v_{\lambda,y}$ component. This indicates that even at a narrow width of 20 nm, phonons with $\Lambda_y < W$ can still make a considerable contribution to thermal transport.

To analyze ballistic transport between channel walls in narrow channels with widths of 20 and 50 nm, we calculate the cumulative thermal conductivity within narrow channels as a function of intrinsic Λ_y, using *ab initio* Monte Carlo simulations, as shown in Fig. 4(e). The cumulative thermal conductivity is normalized by the total thermal conductivity of the channels, which decreases with decreasing W. At $W = 50$ nm, 90% of the thermal conductivity is contributed by phonons with $\Lambda_y < W$, and the fraction increases to 93% at $W = 20$ nm, indicating that phonons with $\Lambda_{\lambda,y} < W$ dominate heat transport at this

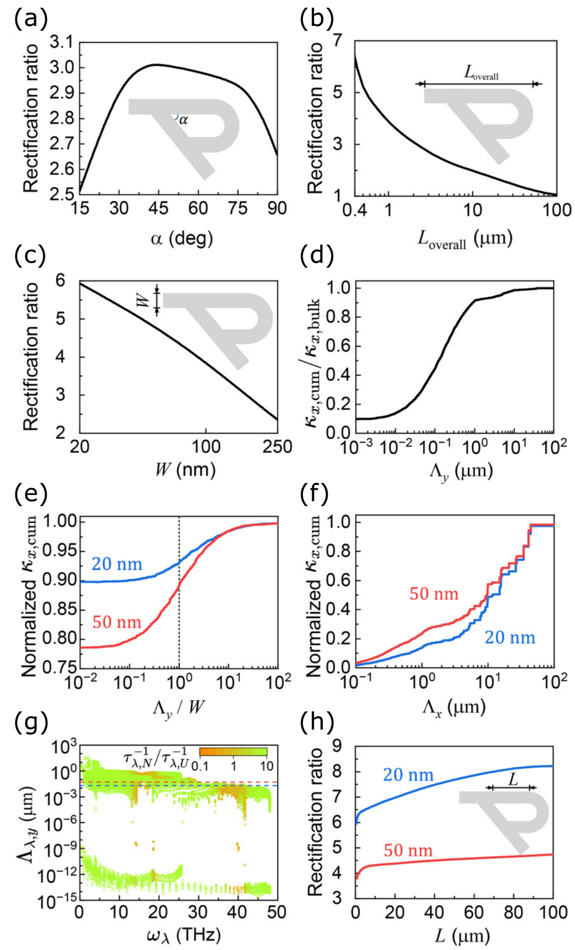

FIG. 4. Geometric parameter dependence of phonon Tesla valve rectification ratio. (a) Rectification ratio as a function of angle α. (b) Rectification ratio as the dimensions are uniformly scaled down, with the degree of scaling represented by the valve overall length L_{overall}. (c) Rectification ratio as a function of W. (d) Normalized cumulative bulk thermal conductivity along the channel $\kappa_{x,\text{cum}}$ as a function of mean free path component perpendicular to channel wall Λ_y. (e) Cumulative channel thermal conductivity $\kappa_{x,\text{cum}}$ as a function of Λ_y/W for narrow channels with $W = 20$ nm (blue) and $W = 50$ nm (red), normalized by the total thermal conductivity of the channel. (f) Cumulative channel thermal conductivity $\kappa_{x,\text{cum}}$ as a function of the mean free path component parallel to the channel walls Λ_x, for narrow channels with $W = 20$ nm (blue) and $W = 50$ nm (red), considering only phonons with $\Lambda_{\lambda,y} < W$ and normalized by their total contribution to κ_x. (g) Mode-dependent $\Lambda_{\lambda,y}$, with the color bar presenting the ratio of normal scattering rate $\tau^{-1}_{\lambda,N}$ to Umklapp scattering rate $\tau^{-1}_{\lambda,U}$. The dashed blue and red lines indicate 20 and 50 nm, respectively. (e) Increase of rectification ratio with increase of L for $W = 20$ nm (blue) and $W = 50$ nm (red). $\alpha = 45°$ in (b),(c),(h).

scale. Although modes with $\Lambda_{\lambda,y} > W$ are the majority in narrow channels, their transport is strongly impeded by diffusive boundary scattering, making a limited contribution to heat conduction.

To further evaluate how far the phonons with $\Lambda_{\lambda,y} < W$ can travel before undergoing anharmonic scattering, we calculate their cumulative contribution to κ_x of the channel as a function of their intrinsic Λ_x, with the use of *ab initio* Monte Carlo simulations. Only phonons with $\Lambda_{\lambda,y} < W$ are considered in the cumulative integration, and the results are normalized by their total contribution to κ_x. As shown in Fig. 4(f), most of the heat conduction from these phonons is contributed by phonons with Λ_x ranging from 1 to 50 μm. This result indicates that many phonon modes with $\Lambda_{\lambda,y} < W$ can travel long distances of up to tens of micrometers before experiencing anharmonic scattering, which means a considerable portion of phonons travel nearly parallel to the channel wall and rarely scatter from the boundary.

The increased γ at reduced W is attributed primarily to the increased forward-backward contrast in the interactions between the nonequilibrium phonons (from the inlet) and the structural boundaries. As W decreases, thermal resistance increases in both the forward direction and the backward direction due to enhanced boundary scattering, but the increase is more significant in the forward direction. In narrow channels, the heat conduction is dominated by the phonons that travel nearly parallel to the channel walls, as other modes are suppressed. In the forward direction, the portion of phonons propagating nearly parallel to the walls of channel I experience significant boundary scattering at the U-turn, where they are redistributed toward equilibrium. Once redistributed, these phonons no longer travel parallel to the walls and are more likely to hit the boundary again, especially as the channel width reduces. In contrast, in the backward direction, nonequilibrium phonons pass through channel II directly, experiencing less boundary scattering compared with the forward direction. As a result, reducing W leads to a greater increase in boundary scattering for the forward flow than for the backward flow. The asymmetric valve structure induces distinct nonequilibrium phonon transport and boundary scattering behaviors between the forward and backward directions, with the contrast becoming more pronounced at smaller channel widths, thereby increasing γ as W decreases.

Figure 4(g) compares $\Lambda_{\lambda,y}$ with W for each phonon mode, where green indicates phonon modes dominated by normal scattering and orange represents modes dominated by Umklapp scattering. At $W = 20$ nm (dashed blue line), although most phonon modes (55%) have $\Lambda_{\lambda,y} > W$, their contributions to thermal transport are significantly suppressed, as ballistic processes between diffusive walls are inefficient for heat transfer. About 11% of the modes have $\Lambda_{\lambda,y} < 20$ nm and stronger normal scattering than Umklapp scattering, where strong normal processes favor forward scattering with a small deflection angle, thereby increasing the deviation of the phonon distribution from the equilibrium Bose-Einstein distribution. Around 2% of phonon modes have $\Lambda_{\lambda,y} < 0.1$ nm, as their group velocities are nearly parallel to the channel walls. Despite accounting for only 2% of the modes, they contribute a dominant 90% of the thermal conductivity within the channel according to *ab initio* Monte Carlo simulations. This large contribution is due to their relatively large $\Lambda_{\lambda,x}$, and their contribution increases in confined channels, as contributions by other modes are suppressed. These results indicate that as the channel width is reduced to 20 nm, phonon transport enters a mixed regime that is partially ballistic and partially hydrodynamic. For most phonon modes, boundary scattering between diffusive channel walls significantly suppresses their contributions to thermal transport. A subset of phonons, however, experience stronger normal scattering than boundary scattering, maintaining a large deviation from the equilibrium Bose–Einstein distribution. Meanwhile, a small fraction of phonons with velocities nearly parallel to the channel walls contribute significantly to thermal transport within the confined geometry.

To examine the influence of channel I length, we vary L while keeping other geometric parameters fixed, i.e., $R = 20$ nm, $\alpha = 45°$, and $W = 20$ nm or $W = 50$ nm. As shown in Fig. 4(h), γ increases with increasing L, since R_f increases with the extended length of channel I, while R_b remains nearly unchanged due to the fixed length of channel II. Since the heat conduction within a 20-nm-wide channel is carried mainly by phonons with $\Lambda_{\lambda,x}$ ranging from 0.1 to 50 μm [Fig. 4(f)], extending L within the same range of $\Lambda_{\lambda,x}$ allows a larger portion of nonequilibrium phonons originating from the inlet boundary to scatter internally before reaching the U-turn, causing R_f to increase with increasing L. Strong normal scattering causes R_f to keep increasing for greater L, even beyond the range of Λ_λ. Therefore, γ continues to increase with increasing L, even when L is already thousands of times larger than W. Moreover, the increase in γ with increasing L becomes more pronounced at smaller channel widths. At $W = 20$ nm, γ increases from 6.5 to 8.2 as L increases from 5 to 100 μm, whereas at $W = 50$ nm, γ increases more slowly from 4.2 to 4.75 over the same range of L. The faster rise at narrower widths is attributed to the larger thermal resistance per unit length, caused by stronger boundary scattering that more effectively impedes the phonon flow.

As the rectification effect largely relies on the diffusive boundary scattering between nonequilibrium phonons and the channel walls, the boundary condition plays a critical role in enabling rectification. To quantitatively assess the impact of boundary conditions, we calculate γ for the valve geometry in Fig. 2 under specular boundary conditions, where phonons undergo mirror reflection at the channel walls. When the boundaries become specular, γ approaches 1, demonstrating that diffusive boundary scattering is essential for rectification. In valves where the channel length is shorter than the phonon mean free path, phonons retain their nonequilibrium distributions up to

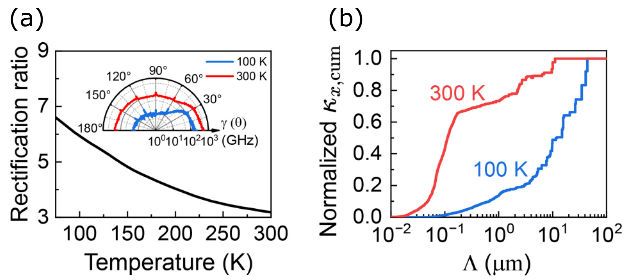

FIG. 5. Temperature dependence of phonon Tesla valve rectification. (a) Temperature-dependent rectification ratio for a valve with $L = 0.3$ μm and $W = 20$ nm. The inset shows the scattering rates as a function of scattering angle θ for graphite at 100 and 300 K. (b) Cumulative thermal conductivity $\kappa_{x,\mathrm{cum}}$ along a 20-nm-wide channel as a function of phonon mean free path Λ at 100 and 300 K.

the U-turn. In the absence of diffusive boundary scattering to redistribute phonons toward equilibrium, the relaxation induced by the scattering between nonequilibrium phonons and asymmetric structural boundaries diminishes forward-backward contrast, resulting in near-vanishing rectification.

Temperature is another key factor affecting the rectification effect, as it alters the phonon scattering. To study the temperature effect, the temperature-dependent γ is calculated for the valve with $\alpha = 45°$, $L = 0.3$ μm, $R = 20$ nm, and $W = 20$ nm. As shown in Fig. 5(a), γ decreases with increasing temperature. This trend arises from the overall increase in scattering rates and the growing Umklapp processes at elevated temperatures. The increased scattering rates dampen the directional propagation of nonequilibrium phonons. Moreover, the growing Umklapp processes lead to a more uniform distribution of phonon propagation directions after scattering, as shown in the inset in Fig. 5(a). The increased isotropy in phonon scattering suppresses the driftlike directional transport of nonequilibrium phonons, thereby reducing γ.

Although phonon scattering becomes stronger and more isotropic at higher temperatures, Fig. 5(a) shows that γ is still around 3 at 300 K. This persistence of rectification at 300 K can be understood from the mean free path distribution of the phonons that contribute to heat transport in a 20-nm-wide channel. Figure 5(b) presents $\kappa_{x,\mathrm{cum}}$ of a 20-nm-wide channel as a function of phonon mean free path Λ at 100 and 300 K. While increase of the temperature from 100 to 300 K dramatically reduces Λ, even at 300 K, about 30% of κ_x in the 20-nm-wide channel is still contributed by phonons with $\Lambda > 0.4$ μm, which is comparable to or longer than the overall valve length. As a result, a substantial fraction of heat is carried by large-Λ phonons, which are able to traverse the valve ballistically. In the forward direction these phonons experience strong diffusive boundary scattering at the U-turn, whereas in the backward direction they travel more directly through the valve with less boundary scattering. This contrast in relaxation between forward and backward transport persists at 300 K, giving γ of around 3 at room temperature.

B. Multistage valve

To further increase the rectification ratio, we use multistage configurations. Figures 6(a) and 6(b) show heat flux maps of a two-stage phonon Tesla valve with $\alpha = 15°$ and $W = 100$ nm. In the forward direction [Fig. 6(a)], a large portion of heat flux meanders through channel I. The sharp turn at the junction between the two stages impedes phonon flow, causing more phonons to return through channel II. The interaction between the forward flow from the inlet and the backward flow from channel II creates a locally circulating phonon flux within channel II, which further blocks phonons from entering channel II from the inlet. In the backward direction [Fig. 6(b)], most of the heat flux takes a relatively straight path through channel II. The corresponding γ increases from 2.51 for the single-stage configuration to 4.67 for the two-stage configuration.

With further increase of the stage number n, the rectification ratio can be estimated through the series thermal resistance model

$$\gamma = \frac{nR_1 + (n-1)R_{1,c}}{nR_2 + (n-1)R_{2,c}}, \tag{5}$$

where R_1 and R_2 are the thermal resistances of the single-stage configuration for the forward and backward directions, respectively, and $R_{1,c}$ and $R_{2,c}$ represent the thermal resistances resulting from the coupling between neighboring stages in the forward and backward directions respectively, and can be determined from the two-stage resistances.

As the number of stages increases, γ continues to rise, converging to an exceptional 10 for 15° valves, as shown in Fig. 6(c). As the number of stages increases, γ of the 15° valves gradually exceeds that of the 45° valve due to the flow dynamics at the stage junctions, i.e., the sharper turning at the stage junctions in the forward direction causes higher $R_{1,c}$, while milder turning in the backward direction results in relatively smaller $R_{2,c}$. As more stages are added, the increased number of stage junctions results in a higher γ value for the 15° valve than for the 45° valve. Since decreasing α results in sharper turns in the forward direction and milder turns in the backward direction, γ increases with decreasing α for infinite-stage valves, as shown in Fig. 6(d).

γ of infinite-stage valves exhibits similar trends with respect to size and channel I length as observed in single-stage valves. In Fig. 6(e), γ increases as the dimensions uniformly scale down, with the degree of scaling represented by the overall length of each stage L_{stage}. γ reaches 12 for the 15° valve and 8 for the 45° valve. In Fig. 6(f),

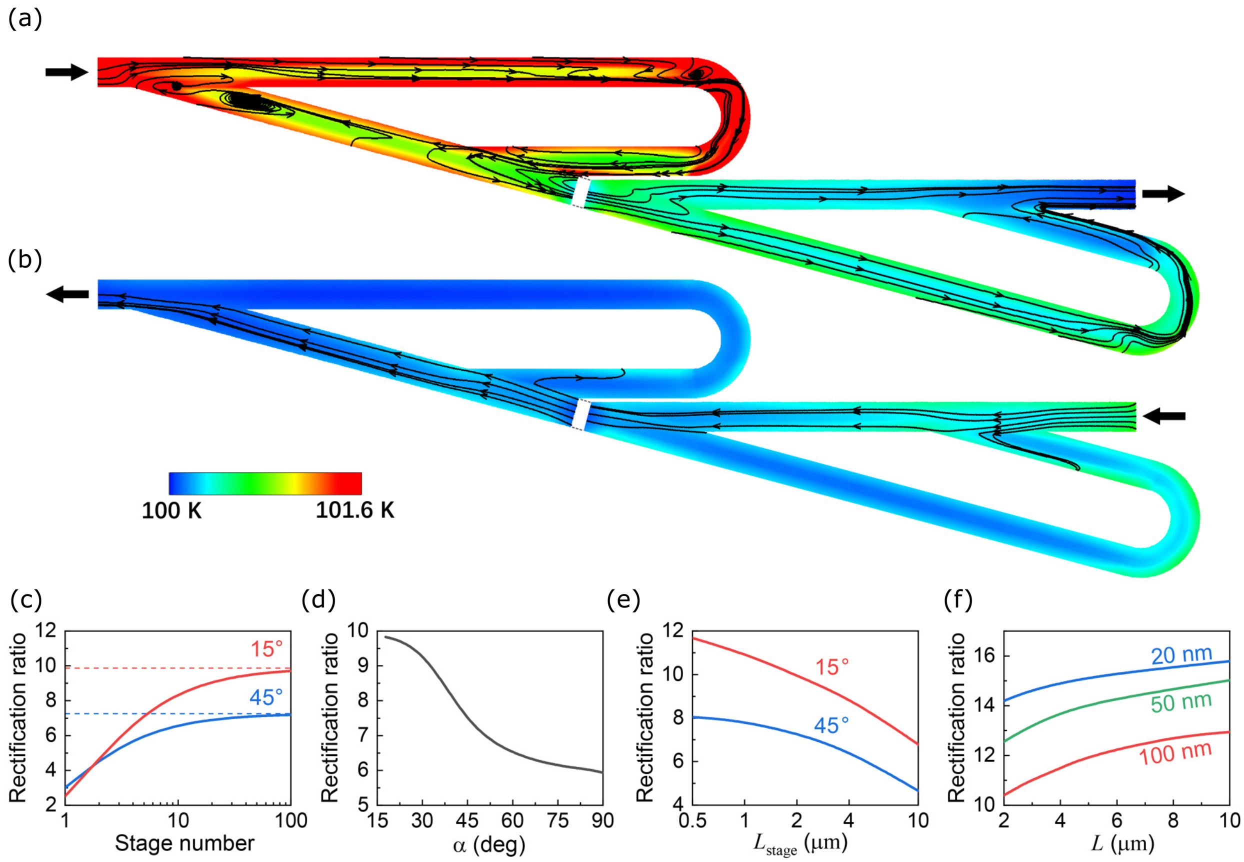

FIG. 6. Multistage thermal Tesla valve. (a),(b) Temperature distribution and heat flux streamlines under a heat power of 1 mW at the inlet boundary for (a) forward flow and (b) backward flow. The color map shows the temperature, the curves represent the streamlines, and the arrows indicate the flow directions. (c) Rectification ratio as a function of the stage number for $\alpha = 15°$ (red) and $\alpha = 45°$ (blue). (d) Rectification ratio as a function of α for infinite-stage valves. (e) Rectification ratio as the dimensions are scaled down for infinite-stage valves with $\alpha = 15°$ (red) and $\alpha = 45°$ (blue), with the degree of scaling represented by the overall length of each stage L_{stage}. (f) Rectification ratio as a function of L for infinite-stage valves with $W = 20$ nm (blue), $W = 250$ nm (green), and $W = 2100$ nm (red). $W = 100$ nm in (a)–(d) and $\alpha = 15°$ in (f).

γ further increases with the lengthened channel I, reaching 16 when L increases to 10 μm for $\alpha = 15°$ and $W = 20$ nm.

C. Phonon Tesla valve versus fluid Tesla valve

While the phonon Tesla valve draws conceptual inspiration from its fluid counterpart, the underlying transport mechanisms are fundamentally different due to the distinct nature of the carriers, i.e., phonons versus molecules.

In fluid Tesla valves, rectification arises primarily from the interplay between mass inertia and geometric asymmetry. As momentum is conserved in intermolecular interactions, strong advection can persist in both the forward direction and the backward direction. Although the fluid velocity vanishes at the walls due to no-slip boundary conditions, the flow strictly obeys mass conservation and thus cannot relax to local equilibrium, i.e., a Maxwell-Boltzmann distribution with zero average velocity. As a result, the fluid maintains a high drift velocity throughout the entire structure, regardless of the forward or backward directions. This sustained bulk motion limits the contrast in flow resistance between forward and backward directions, thereby limiting γ.

By contrast, phonons are quasiparticles that do not require particle number conservation; therefore, they are allowed to relax toward the equilibrium distribution without maintaining a persistent drift velocity. In the forward direction, a large portion of nonequilibrium phonons relax toward equilibrium due to the longer length of channel I compared with channel II, as well as strong boundary scattering at the U-turn. In the backward direction, phonons can pass through the channel more directly with less scattering, thus maintaining nonequilibrium and drifting character. This forward-backward contrast in relaxation results in a substantial difference in thermal resistance between the forward and backward directions, thereby enabling strong thermal rectification.

The key distinction lies in the nature of the carriers: fluid molecules are real particles that follow mass conservation, whereas phonons are quasiparticles that do not require particle number conservation. This fundamental difference allows nonequilibrium phonons to gradually relax toward equilibrium via scattering, particularly in the forward direction. In contrast, fluids maintain a large drift velocity throughout the entire valve structure in both directions, which limits the resistance difference between forward and backward directions.

VI. SUMMARY

We introduced a thermal rectifier using the collective driftlike phonon transport in graphite combined with the Tesla valve design. Through *ab initio* Monte Carlo simulations, we systematically investigated the geometric effect and achieved a significant thermal rectification ratio of up to approximately 8 for a single-stage valve and approximately 16 for a multistage valve, significantly exceeding the values of state-of-the-art solid-state thermal rectifiers. Our findings illuminate a pathway to manipulate heat, potentially revolutionizing energy conversion, waste-heat utilization, and thermal management.

ACKNOWLEDGMENTS

Y.H. acknowledges partial support from the DOE Office of Science, Office of Basic Energy Sciences and Office of Fusion Energy Sciences, as part of Co-design and Heterogeneous Integration in Microelectronics for Extreme Environments Center, a Microelectronics Science Research Center; from NSF Grant No. DMR-1753393, and from NIGMS Grant No. R35GM147391. This work used computational and storage services associated with the Hoffman2 Shared Cluster provided by the UCLA Office of Advanced Research Computing's Research Technology Group, and the Bridges-2 at Pittsburgh Supercomputing Center through allocation DMR180111 from the Advanced Cyberinfrastructure Coordination Ecosystem: Services & Support program, which was supported by NSF Grants No. 2138259, No. 2138286, No. 2138307, No 2137603, and No. 2138296.

DATA AVAILABILITY

The data that support the findings of this article are not publicly available. The data are available from the authors upon reasonable request.

APPENDIX A

The inlet and outlet areas and boundaries are defined in Fig. 7.

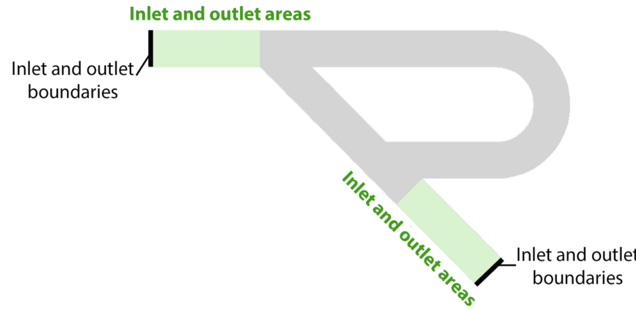

FIG. 7. The inlet and outlet areas and boundaries in the phonon Tesla valve. The designation of inlet and outlet depends on the forward or backward direction of flow.

[1] M. Li, S. Li, Z. Zhang, C. Su, B. Wong, and Y. Hu, Advancing thermal management technology for power semiconductors through materials and interface engineering, Acc. Mater. Res. **6**, 563 (2025).

[2] Y. Cui, M. Li, and Y. Hu, Emerging interface materials for electronics thermal management: experiments, modeling, and new opportunities, J. Mater. Chem. C **8**, 10568 (2020).

[3] S. Chu and A. Majumdar, Opportunities and challenges for a sustainable energy future, Nature **488**, 294 (2012).

[4] S. Li, C. Su, Z. Qin, A. Alatas, M. Kunz, T. Yamada, S. D. Kelly, M. H. Upton, A. Gironda, J. Zhao, B. Kalkan, W. Yang, T. Aoki, and Y. Hu, Metallic θ-phase tantalum nitride has a thermal conductivity triple that of copper, Science **391**, 707 (2026).

[5] J. S. Kang, M. Li, H. Wu, H. Nguyen, and Y. Hu, Experimental observation of high thermal conductivity in boron arsenide, Science **361**, 575 (2018).

[6] J. S. Kang, M. Li, H. Wu, H. Nguyen, T. Aoki, and Y. Hu, Integration of boron arsenide cooling substrates into gallium nitride devices, Nat. Electron. **4**, 416 (2021).

[7] S. Li, Z. Qin, H. Wu, M. Li, M. Kunz, A. Alatas, A. Kavner, and Y. Hu, Anomalous thermal transport under high pressure in boron arsenide, Nature **612**, 459 (2022).

[8] M. Li, H. Wu, E. M. Avery, Z. Qin, D. P. Goronzy, H. D. Nguyen, T. Liu, P. S. Weiss, and Y. Hu, Electrically gated molecular thermal switch, Science **382**, 585 (2023).

[9] G. Wehmeyer, T. Yabuki, C. Monachon, J. Wu, and C. Dames, Thermal diodes, regulators, and switches: Physical mechanisms and potential applications, Appl. Phys. Rev. **4**, 041304 (2017).

[10] T. Swoboda, K. Klinar, A. S. Yalamarthy, A. Kitanovski, and M. Muñoz Rojo, Solid-state thermal control devices, Adv. Electron. Mater. **7**, 2000625 (2021).

[11] Z. Qin, M. Li, J. Flohn, and Y. Hu, Thermal management materials for energy-efficient and sustainable future buildings, Chem. Commun. **57**, 12236 (2021).

[12] N. Tesla, *Valvular Conduit*, US Patent 1329559 (1920).

[13] X. Huang, R. Anufriev, L. Jalabert, K. Watanabe, T. Taniguchi, Y. Guo, Y. Ni, S. Volz, and M. Nomura, A graphite thermal Tesla valve driven by hydrodynamic phonon transport, Nature **634**, 1086 (2024).

[14] C. Su, H. Wu, L. Dai, Z. Zhang, S. Li, and Y. Hu, Nonclassical heat transfer and recent progress, J. Heat Mass Transfer **147**, 032502 (2025).

[15] J. C. Ward and J. Wilks III, Second sound and the thermo-mechanical effect at very low temperatures, London Edinburgh, Dublin Philos. Mag. J. Sci. **43**, 48 (1952).

[16] E. W. Prohofsky and J. A. Krumhansl, Second-sound propagation in dielectric solids, Phys. Rev. **133**, A1403 (1964).

[17] R. J. Hardy, Phonon Boltzmann equation and second sound in solids, Phys. Rev. B **2**, 1193 (1970).

[18] A. Cepellotti, G. Fugallo, L. Paulatto, M. Lazzeri, F. Mauri, and N. Marzari, Phonon hydrodynamics in two-dimensional materials, Nat. Commun. **6**, 6400 (2015).

[19] S. Lee, D. Broido, K. Esfarjani, and G. Chen, Hydrodynamic phonon transport in suspended graphene, Nat. Commun. **6**, 6290 (2015).

[20] H. Wu and Y. Hu, Ab initio investigations on hydrodynamic phonon transport: From diffusion to convection, Int. J. Heat Mass Transfer **220**, 124988 (2024).

[21] M. Simoncelli, N. Marzari, and A. Cepellotti, Generalization of Fourier's law into viscous heat equations, Phys. Rev. X **10**, 11019 (2020).

[22] F. P. Incropera, D. P. DeWitt, T. L. Bergman, and A. S. Lavine, *Fundamentals of Heat and Mass Transfer* (Wiley, Hoboken, NJ, 2017).

[23] G. P. Srivastava, *The Physics of Phonons* (CRC Press, New York, 1990).

[24] S. Huberman, R. A. Duncan, K. Chen, B. Song, V. Chiloyan, Z. Ding, A. A. Maznev, G. Chen, and K. A. Nelson, Observation of second sound in graphite at temperatures above 100 K, Science **364**, 375 (2019).

[25] Y. Machida, N. Matsumoto, T. Isono, and K. Behnia, Phonon hydrodynamics and ultrahigh–room-temperature thermal conductivity in thin graphite, Science **367**, 309 (2020).

[26] X. Huang, Y. Guo, Y. Wu, S. Masubuchi, K. Watanabe, T. Taniguchi, Z. Zhang, S. Volz, T. Machida, and M. Nomura, Observation of phonon Poiseuille flow in isotopically purified graphite ribbons, Nat. Commun. **14**, 2044 (2023).

[27] See Supplemental Material http://link.aps.org/supplemental/10.1103/bgr6-wryy for details of the derivation of the scattering matrix and Ziman's model of specular reflection probability.

[28] H. Wu, H. Fan, and Y. Hu, Ab initio determination of ultrahigh thermal conductivity in ternary compounds, Phys. Rev. B **103**, L041203 (2021).

[29] T. Tadano, Y. Gohda, and S. Tsuneyuki, Anharmonic force constants extracted from first-principles molecular dynamics: Applications to heat transfer simulations, J. Phys.: Condens. Matter **26**, 225402 (2014).

[30] P. Hohenberg and W. Kohn, Inhomogeneous electron gas, Phys. Rev. **136**, B864 (1964).

[31] W. Kohn and L. J. Sham, Self-consistent equations including exchange and correlation effects, Phys. Rev. **140**, A1133 (1965).

[32] P. Giannozzi, S. Baroni, N. Bonini, M. Calandra, R. Car, C. Cavazzoni, D. Ceresoli, G. L. Chiarotti, M. Cococcioni, I. Dabo, *et al.*, QUANTUM ESPRESSO: A modular and open-source software project for quantum simulations of materials, J. Phys.: Condens. Matter **21**, 395502 (2009).

[33] P. Giannozzi, O. Andreussi, T. Brumme, O. Bunau, M. B. Nardelli, M. Calandra, R. Car, C. Cavazzoni, D. Ceresoli, M. Cococcioni, *et al.*, Advanced capabilities for materials modelling with Quantum ESPRESSO, J. Phys.: Condens. Matter **29**, 465901 (2017).

[34] We used the pseudopotential C.pbe-n-kjpaw_psl.1.0.0.UPF from http://www.quantum-espresso.org.

[35] J. Klimeš, D. R. Bowler, and A. Michaelides, Van der Waals density functionals applied to solids, Phys. Rev. B **83**, 195131 (2011).

[36] C. D. Landon and N. G. Hadjiconstantinou, Deviational simulation of phonon transport in graphene ribbons with ab initio scattering, J. Appl. Phys. **116**, 163502 (2014).

[37] J. S. Kang, H. Wu, and Y. Hu, Thermal properties and phonon spectral characterization of synthetic boron phosphide for high thermal conductivity applications, Nano. Lett. **17**, 7507 (2017).

[38] J. M. Ziman, *Electrons and Phonons: The Theory of Transport Phenomena in Solids* (Oxford University Press, London, 1960).